Out-of-Equilibrium Measurements of Kinetic Constants on a Biosensor

Donatien Mottin, Florence Razan, Claude Nogues, Marie-Caroline Jullien

Out-of-Equilibrium Measurements of Kinetic Constants on a Biosensor

Donatien Mottin,[†,‡] Florence Razan,[‡] Claude Nogues,[¶] and Marie-Caroline Jullien[*,†]

†*Univ. Rennes 1, CNRS, IPR (Institut de Physique de Rennes) UMR 6251, F-35000 Rennes*

‡*ENS Rennes, SATIE, UMR-CNRS 8029, Campus de Ker Lann, F-35170 Bruz*

¶*ENS Paris-Saclay, LBPA UMR-CNRS 8113, Gif-sur-Yvette, France*

E-mail: marie-caroline.jullien@univ-rennes1.fr

Phone: +33 2 23 23 78 52

Abstract

Conventional measurements of kinetic constants currently in use are performed at equilibrium and may require large volumes, especially at low association rate constant k_{on}. If the measurements are made out of equilibrium, the values obtained may be biased by dilution of the sample with the flow of the running buffer. In some applications, the available sample volume can be very critical and requires the development of tools to measure kinetic constants with low volumes. In this paper, through experimental, numerical simulation and a modeling combined approach, we propose a SPR-based method that relies on an out-of-equilibrium measurement, using the effect of dilution by flow to its advantage. This new method should have a significant impact in biochemistry and medical research.

The efficiency of a complex formed from two interacting molecules is intrinsically linked

to the characteristic time of formation of the complex. Many biological mechanisms are based on complexation: antibody-antigen interacting for immune reaction[1] or complementary single-stranded DNA hybridization to form DNA double helix[2] for instance. In this context, the complexation reaction is a key element of many modern bioanalysis protocols such as immunoassays on chip,[3–7] cancer point-of-care diagnostics[8,9] or, more generally, biosensing.[10–12] This reaction is quantitatively described through three quantities: the association rate constant k_{on}, which describes how fast two interacting molecules form a complex at a given concentration, the dissociation rate constant k_{off}, which describes the time it takes for a complex to dissociate, and the equilibrium dissociation constant $K_D = \frac{k_{\text{off}}}{k_{\text{on}}}$ which describes the affinity between the two interacting molecules.

Different strategies have been developed to measure these constants like static methods and methods under flow to cite a few. A typical example of static methods is ELISA, that can be performed by grafting on of the two molecules on plate wells, the other one being in solution at various concentrations. The measure of K_D is performed at equilibrium using colorimetric measurements.[13–18] Concerning methods under flow, we can cite two approaches. In a first one, both molecules are no longer grafted on a surface, such as in the capillary electrophoresis method, in which the analysis is based on the mobility difference between the molecules and the formed complexes under an electrical field.[19–24] In the second approach, one of the two molecules is grafted on a surface, while the second one is injected using a flow and passed though the biochip surface. In this paper we focus on this last strategy.

The methodology is based on grafting a ligand on a sensitive surface and flowing an interacting target continuously above this surface. By analysing the time evolution of the number of complexes that are formed, named sensorgram, one can thus extract k_{on} and k_{off} values. Classical methods used to obtain such sensorgrams are typically based on Surface Plasmon Resonance (SPR),[25–28] Quartz Crystal Microbalance (QCM),[29,30] electrochemistry[31,32] or other label-free methods.[33] However, sample plugs can be distorted by the flow and, combined to diffusion, this leads to the Taylor-Aris dispersion,[34,35] a classical hydrodynamic

effect that modifies the bulk concentration and tends to bias the sensorgrams. Generally, this hydrodynamic effect can be disregarded by working at equilibrium, typically using the Langmuir isotherm method.

The Langmuir isotherm method is based on the classical model used to describe association and dissociation of targets on a ligand-recovered surface known as the first-order Langmuir kinetics:

$$\frac{ds}{dt} = k_{\text{on}} c_0 (s_m - s) - k_{\text{off}} s \tag{1}$$

in which the temporal evolution of the number of complexes s, formed over the initial total number of free ligands s_m, results from two mechanisms: association $\frac{ds}{dt}|_{\text{on}} = k_{\text{on}} c_0 (s_m - s)$ and dissociation of complexes $\frac{ds}{dt}|_{\text{off}} = -k_{\text{off}} s$, at a given target concentration c_0. At equilibrium, the two contributions balance and the sum of these two rates is equal to zero, *i.e.* $s_{\text{eq}} = s_m \dfrac{c_0}{c_0 + k_{\text{off}}/k_{\text{on}}}$. In practice, the number of complexes s_{eq} at equilibrium is measured for different initial concentrations c_0, and $K_D = k_{\text{off}}/k_{\text{on}}$, the equilibrium dissociation constant, then appears as a fitting parameter of the curve.

Although this method provides accurate measurements, working at equilibrium can require an increasing volume of sample while k_{on} decreases. In fact, working under flow implies a continuous injection, and thus continuous target supply. The smaller the k_{on} value is, the longer it takes to reach equilibrium. Thus, equilibrium methods may require massive amounts of sample for especially low k_{on} molecules. To lower the sample volume, a first strategy consists in flowing a small volume sample back and forth above the sensing surface, still working at equilibrium.[36]

In this paper, we propose a second strategy built on an out-of-equilibrium SPR-based method to calculate the k_{on} value of a given complex. Instead of relying solely on the equilibrium measurements, we take advantage of a dynamical measurement for which the number of formed complexes increases with time in order to extract the k_{on} values. As this is an out-of-equilibrium measurement, the Taylor-Aris dispersion, explained in the paper, plays a significant role. We propose a method of analysis which makes it possible to interpret the

measurements by taking this mechanism into account. Reaching the equilibrium is thus no longer required to get accurate k_{on} values. With this new method, analysis time and sample volume can be significantly reduced, especially for the lowest k_{on}. Typically, in our parameter range, the gain in analysis time is about 200 and the gain in volume is about 40. This method can have a huge impact on kinetics analysis of slowly interacting proteins, such as the metalloproteins, *i.e.* low k_{on} metal-binding proteins, that have been identified as an essential element in cancer pathology.[37–42]

In this paper, we first present our experimental results, probing the influence of Taylor-Aris dispersion on out-of-equilibrium measurements. Then, we present numerical simulations reproducing the experimental measurements. The agreement between experimental and numerical results allows us to confirm our hypothesis on the effect of the Taylor-Aris dispersion, leading to a new model described in the third part. Finally, we discuss the range of validity of the model. In routine use, it is simply necessary to solve two equations which depend only on the parameters of the experiment (geometry, hydrodynamic parameters, concentration, surface density of ligands) which makes the measurement very simple.

For sakes of homogeneity, we use the SI units for k_{on} throughout the paper ($\mathrm{m^3\ mol^{-1}\ s^{-1}}$) and not its usual unit ($\mathrm{L\ mol^{-1}\ s^{-1}}$).

Experimental

Injection protocole

The experiments are performed using a SPRi-Plex Horiba apparatus. The procedure is skteched on Figure 1. A sample (in red) of volume V_0, length L_0 and target concentration $c_0 = 50$ nM in a 400 mM Phosphate Buffer Saline aqueous solution (PBS, pH = 7.4), is injected in a capillary tubing of radius $R = 300\ \mu$m. This plug is pushed by a target-free PBS solution through a capillary tubing of radius R and length $L_1 = 28.4$ cm at a flow rate Q, and reaches a microfluidic system, of height $H = 1.75$ mm and width $W = 8.9$ mm,

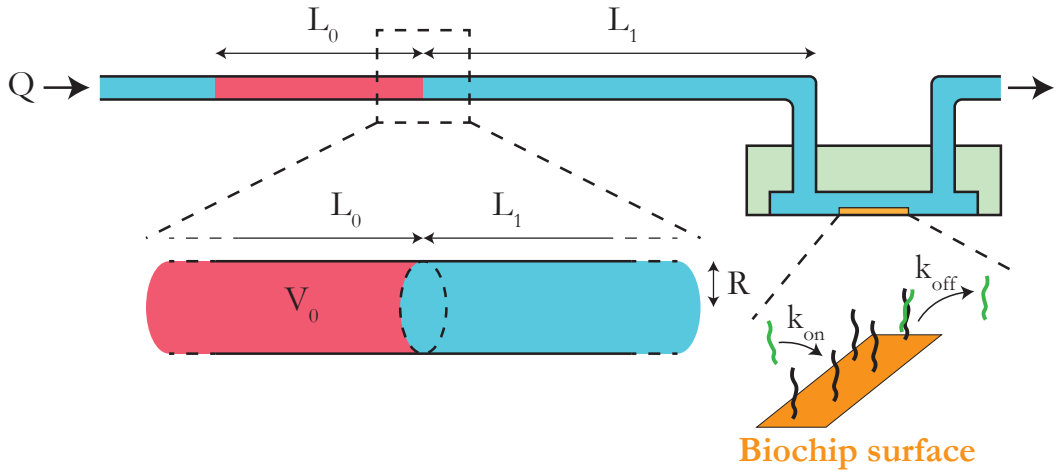

Figure 1: **Sketch of the Measurement System.** (Red) Sample of volume V_0, length L_0 and target concentration c_0, injected in a capillary tubing of radius R at a flow rate Q. (Blue) Buffer. (Yellow) Biochip sensitive surface located in the microfluidic chamber, recovered by ligands. An analysis system monitors the amount of formed complex versus time. The sktech is not a the scale.

in which a functionnalized gold biochip surface (sensitive surface) has been integrated (in yellow on Figure 1). The temperature is fixed at 25.0°C near the biochip surface.

The sample solution contains the target, free single strand DNA (ssDNA); while the ligand, complementary ssDNA, is grafted on the biochip surface (see supporting information for the DNA sequences). The complexes number versus time is measured by SPRi (Surface Plasmon Resonance imaging),[43–45] an optical technique commonly used for biological kinetics measurement.[1,46–49] After each experiment, the biochip surface is regenerated: all the complexes on the biochip surface are dissociated by injecting 200 μL of a Sodium Dodecyl Sulfate (SDS) solution (0.1% w/v[50]) in milliQ water at 50 μL/min. DNA regeneration allows a total dissociation of complexes, thus allowing repeated experiments on non altered surfaces. The SPRi injection valve system and the microfluidic system are then thoroughly washed by several injections of PBS.

Biochip surface treatment

A Horiba SPRi-Biochip^{TM}, composed of a high refractive index glass prism coated with a thin gold film, is subjected to different successive treatments: milliQ water washing, drying

with argon, exposition to UV Ozone for cleaning during 5 minutes followed by a direct immersion in absolute ethanol for a least 20 minutes. Afer drying under argon, a 5' thiolated single-stranded DNA (SH-ssDNA) at 10μM diluted in 400 mM phosphate buffered is spotted as $0.2\,\mu$L drops on the freshly treated gold biochip surface. The ssDNA drops are then left to incubate overnight in a humid chamber. The biochip is further directly introduced in the SPRi instrument and the surface is thoroughly rinsed with the running buffer (Phosphate Buffer Saline, PBS).

Experimental Results

As stated in the introduction, working out-of-equilibrium means that the final state in (1), $s_{\text{eq}} = s_m \dfrac{c_0}{c_0 + k_{\text{off}}/k_{\text{on}}}$, is not reached. The number of complexes is thus negligible compared to the equilibrium one: $s \ll s_{\text{eq}}$. Formally this leads to:

$$k_{\text{on}} c_0 s + k_{\text{off}} s \ll k_{\text{on}} c_0 s_m \tag{2}$$

Then, far from equilibrium, the total complexation rate in equation (1) reduces to:

$$\frac{ds}{dt} = k_{\text{on}} c_0 s_m \tag{3}$$

where c_0 is the target concentration. According to (3), the number of complexes evolves linearly with time. As such, k_{on} value can be extracted from the measure of the complex formation rate $\frac{ds}{dt}$. In the following, we note k_{on} its intrinsic value, independent of the experimental and analysis protocol. Experiments and numerical simulations are performed by varying the experimental parameters and the measured constants are noted $\widetilde{k_{\text{on}}}$, obtained using:

$$\widetilde{k_{\text{on}}} = \frac{1}{c_0 s_m} \frac{ds}{dt}, \tag{4}$$

for which bias can be introduced either by the experimental protocol or the analysis method.

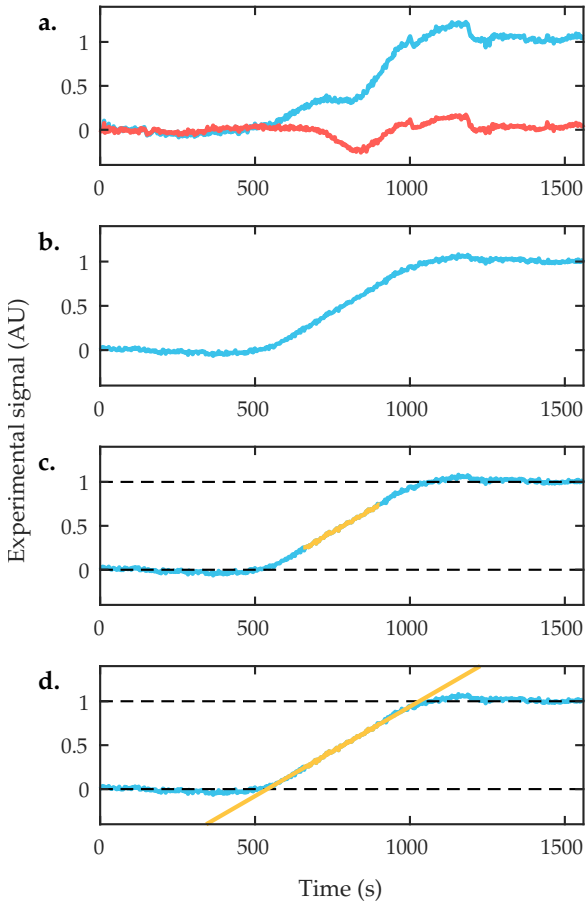

Figure 2: **Signal Analysis Process.** Experimental signal obtained for $R = 300\ \mu$m, $L_1 = 28.4$ cm, $D = 1.27\ 10^{-10}$ m^2/s, $Q = 10\ \mu$L/min, $V_0 = 5\ \mu$L. The sample is injected at $t = 0$, and travels above the biochip surface between $t \simeq 500$ s and $t \simeq 1000$ s. **a.** Raw data. (blue) sample signal, (red) reference signal, recorded at a nearby reference ligand-free surface. **b.** Background subtraction **c.** Selection of the data points forming the linear part of the signal (yellow points). **d.** Linear fitting of the complex formation rate $\frac{ds}{dt}$.

DNA hybridization is used as a model complexation in this study. Its particularly low k_{on} value[2,47] and its zero dissociation rate constant ($k_{\text{off}} = 0$) makes it possible working out-of-equilibrium. Note that working out-of-equilibrium does not require necessarily a $k_{\text{off}} = 0$.

Experiments are performed by tuning the injection flow rate $Q \in [3; 500]\ \mu$L/min and the injected volume $V_0 \in [2; 500]\ \mu$L, while all the other parameters are set fixed (surface treatment, ssDNA ligand concentration s_m, ssDNA target concentration c_0, capillary tubing length L_1, microfluidics chamber geometry, ...). Each set of flowing conditions (flow rate Q and injected volume V_0) is reproduced 7 times. The Reynolds number $R_e = 2Q/(\pi R^2 \nu)$

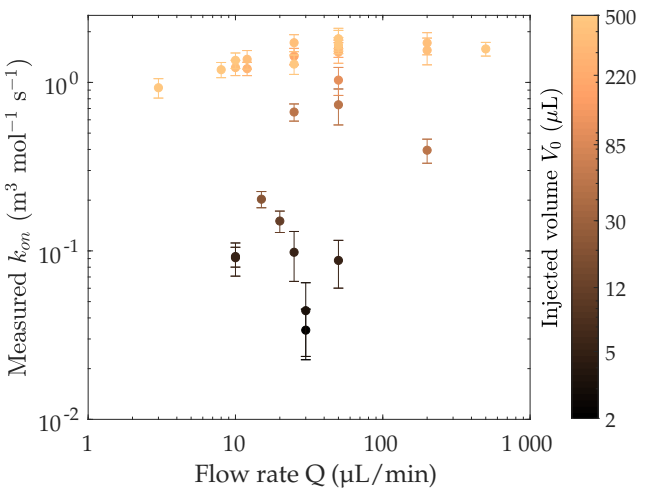

Figure 3: **Variation of the out-of-equilibrium measured $\widetilde{k_{\mathrm{on}}}$ for various injection flow rates Q and injected sample volume V_0.** Each point represents the mean result of 7 experiments with the same parameter sets. Error bars represent the standard deviation among these 7 experiments.

varies between $8\,10^{-2}$ and 13, with ν the kinematic viscosity of the carrier liquid, ensuring laminar flow.

A typical recorded signal is shown on figure 2.a. By subtracting the background signal, a typical sensorgram is recovered as shown on figure 2.b. The complex formation rate $\frac{ds}{dt}$ is extracted by measuring the slope in the linear part of the curve (yellow part of 2.c.d).

Once the complex formation rate is measured, $\widetilde{k_{\mathrm{on}}}$ is computed following (4). Figure 3 displays the different values of the measured $\widetilde{k_{\mathrm{on}}}$ for each of the 29 set of flowing conditions. The fact that the measured values vary over two decades shows that either our experiment has a bias, or that the flow conditions Q and V_0, the only varying parameters, play a major role. We assume that hydrodynamics must considered when working out of equilibrium. Indeed, diffusion alone cannot be responsible for a sufficiently fast dilution to bias the measurements as observed. For example, a sample in a liquid at rest (see Figure 4.a), of volume $V_0 = 10\,\mu$L, with a diffusion coefficient of $D \sim 10^{-10}$ m^2/s (a typical value for the target we use), in a capillary tubing of radius $300\,\mu$m, occupies a capillary tubing length $L_0 = \frac{V_0}{\pi R^2} \simeq 3.5$ cm. To diffuse over a distance $\delta \simeq L_0$, which means diluting in twice its initial volume, it takes a typical diffusive time $t \sim \frac{L_0^2}{D} \sim 10^6$ s, *i.e.* over a week. For most biological molecules, such as

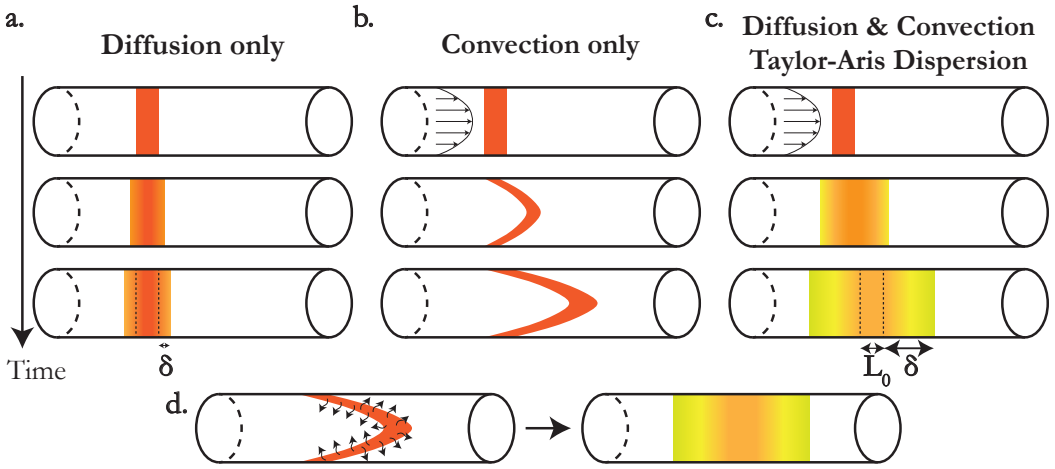

Figure 4: **Illustration of the Taylor-Aris Dispersion Mechanism.** A sample is transported in a capillary tubing where it is submitted to both diffusion and convection by the surrounding liquid. The color represents the target concentration inside the sample (the more concentrated the target, the redder the color). δ is the dilution length, *i.e.* the sample length increase due to its journey in the capillary tubing. **a. Diffusion only.** If the fluid is at rest, the only transport mechanism is diffusion. Targets slowly diffuse in the capillary tubing. **b. Convection only.** If the liquid is in motion, a parabolic flow velocity profile develops in the capillary tubing. Targets in the center of the capillary tubing move much faster than those near the walls. The sample is therefore deformed by the liquid flow. **c. Diffusion and Convection: Taylor-Aris Dispersion.** When both effects are considered, the sample is deformed by convection and then targets spread over the entire height of the capillary tubing by diffusion. This way, the sample dilute itself way faster than by pure diffusion. **d. Simplified Sketch of the Mechanism.**

antibodies, the diffusion coefficient is about $\sim 10^{-12}$ m^2/s leading to a diffusion time about a year. This means that, without a flow, the target concentration does not change during the experiment.

At this stage, it is necessary to consider mass transport in the system, including the combination of both convection in the direction of the flow and diffusion transverse to the flow, see figure 4. Indeed, for a flow at low Reynolds number, the velocity profile has a parabolic shape, the velocity is maximum at the centre of the pipe and zero at the walls, so that a plug sample is distorted as shown in Figure 4.b. Then, the target sample diffuses over the cross-section of the channel as depicted on Figure 4.d. The combination of these two effects results in an enhanced diffusion called the Taylor-Aris dispersion.[34,35] Our working hypothesis is that the discrepancy of the measurements comes from samples more or less

diluted by this dispersion modifying the concentration of the solution arriving at the sensor.

Before deriving a model, we performed numerical simulations, reported in the next section, in order to check that the discrepancy found on the measured association rate constants come from this effect and not from another bias.

Numerical Results

Each experimental conditions are reproduced numerically, using two different numerical approaches, taking only into account the Taylor-Aris dispersion and the surface complexation. To perform these numerical simulations, we implement a k_{on} value and the output of the simulations is the measured $\widetilde{k_{\mathrm{on}}}$ value obtained from the simulated sensorgram. Two different numerical strategies are used in order to ensure the absence of numerical bias. The first one uses COMSOL Multiphysics®, while the second one uses a code developed in our laboratory. This home-made code is a Lagrangian numerical strategy which consists in computing the trajectory of each target at each time step.

In order to simplify the reading of the paper, the details of these simulations are reported in supporting information. Indeed, the results of these simulations allow us to establish our working hypothesis, but the details of their practical realisation is not in the scope of the paper.

Figure 5 displays the results obtained by the two approaches detailed in supporting information. Remarkably, the two simulations reproduce the dispersion of $\widetilde{k_{\mathrm{on}}}$ values observed experimentally.

Since the simulations only take into account the Taylor-Aris dispersion, we hypothesize that it is the only mechanism responsible for the dispersion of the experimentally obtained values. Based on this hypothesis, we will establish a model in the following section and compare it with the experimental and numerical results.

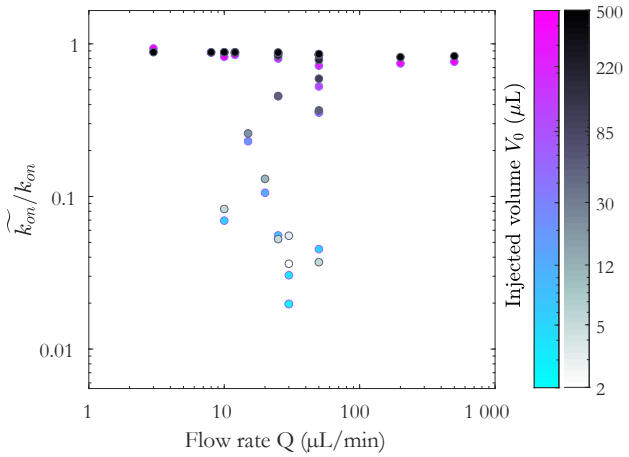

Figure 5: **Variation of the out-of-equilibrium simulated $\widetilde{k_{on}}$ value for various injection flow rates Q and injected sample volume V_0.** COMSOL simulations results (black/white) and Lagrangian simulations results (purple/blue) are both normalized by the input k_{on} value.

Data Analysis Model

In this section, we propose to rationalize the effect of Taylor-Aris dispersion on the out-of-equilibrium complexation kinetics. From Taylor-Aris dispersion, combining axial convection and transverse diffusion, results in an effective diffusion coefficient [34,35] $D_{TA} = D\left(1 + \frac{Q^2}{48\pi^2 D^2 R^2}\right)$. In our experiments with $D \sim 10^{-10}$ m^2/s, for a flow rate about $Q \geq 1\,\mu$L/min, the first term is negligible as long as $R \ll 1$ cm. For antibodies, the diffusion coefficient is about $D \sim 10^{-12}$ m^2/s [51,52] and for the same flow rate, the first term is negligible as long as $R \ll 1$ m. The radius that is used on standard analysis system is much smaller than the two values we found. The effective diffusion thus reduces to:

$$D_{TA} \simeq \frac{Q^2}{48\pi^2 D R^2} \tag{5}$$

It is thus possible to compute the real concentration of the sample when it reaches the biochip surface, taking this hydrodynamic dilution into account. The sample length is initially L_0 and the center of the sample travels over a distance $L_1 + L_0/2$ before reaching the biochip surface (see Figure 1). With a mean travel velocity $U = Q/\pi R^2$, it takes a typical time

$\tau \simeq \frac{L_1+L_0/2}{U}$ to reach the biochip surface. During this time, the sample plug diffuses over a distance δ (see Figure 4):

$$\delta = \sqrt{D_{TA}\tau} = \sqrt{\frac{D_{TA}(L_1 + L_0/2)\pi R^2}{Q}} \tag{6}$$

It is clear from this equation that the flow is responsible for the expansion of the initial plug. A scaling law describing the mean concentration c of the sample above the biochip surface then writes:

$$c \sim c_0 \frac{L_0}{\delta + L_0} \tag{7}$$

where $\frac{L_0}{\delta+L_0}$ is a dilution factor. This dilution factor therefore depends on the flow rate (*via* δ) and the initial volume (*via* L_0). For $\delta \ll L_0$, $c = c_0$, there is no dilution; while for $\delta \gg L_0$, $c = \frac{L_0}{\delta} c_0 \ll c_0$, the sample is diluted and the concentration above the biochip surface is way reduced compared to a non-diluted case.

The exact computation leads to (see supporting information):

$$c = c_0 \,\mathrm{erf}\left(\frac{L_0}{4\delta}\right) \tag{8}$$

where erf is the error function, of asymptotic behavior $\mathrm{erf}\left(\frac{L_0}{4\delta} \ll 1\right) \simeq \frac{L_0}{4\delta}$ and $\mathrm{erf}\left(\frac{L_0}{4\delta} \gg 1\right) \simeq 1$. These asymptotic behaviors recover the solutions found using the scaling law model (7): $c \simeq c_0$ if $\delta \ll L_0$ and $c \ll c_0$ if $\delta \gg L_0$.

From (5), (6) and using $L_0 = \frac{V_0}{\pi R^2}$, we define the hydrodynamic dilution factor ψ as:

$$\boxed{\psi = \frac{4\delta}{L_0} = \frac{R^2}{V_0}\sqrt{\frac{\pi Q\left(L_1 + \frac{V_0}{2\pi R^2}\right)}{3D}}} \tag{9}$$

Then,

$$c = c_0 \mathrm{erf}(1/\psi) \tag{10}$$

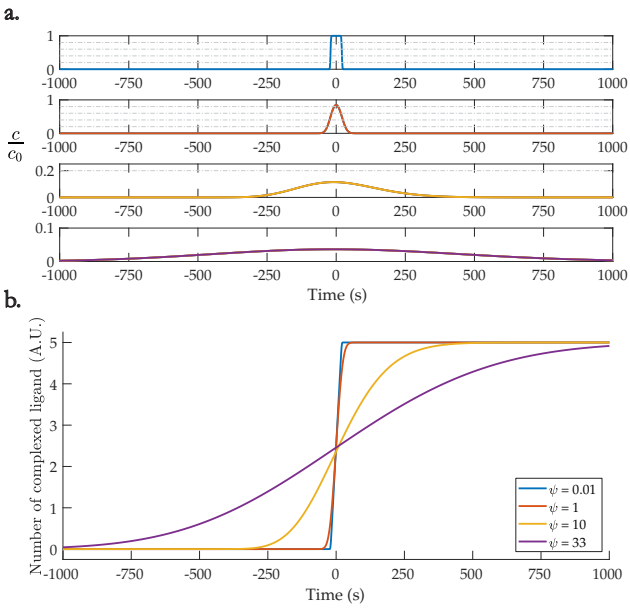

Figure 6: **Analytic predictions for different ψ values.** Color codes for ψ value are represented in the inset of plot (b). At $t = 0$ the barycenter of the sample reaches the biochip. **a.** Temporal evolution of the concentration above the biochip. For dilution factor $\psi < 1$, the concentration profile is not distorted at all, while for $\psi > 1$ the sample is diluted. **b.** Sensorgram allowing to extract the complex formation rate $\frac{ds}{dt}$ from the slopes at the different ψ values. For dilution factor $\psi < 1$, the sample is highly concentrated, the slope of the curve is steep. On the opposite, for $\psi > 1$, the sample is diluted, which results in a smaller slope for the same injection concentration c_0.

The value of ψ provides a quantitative indication of whether or not a sample has been hydrodynamically diluted during its traveling time as depicted on Figure 6a. If $\psi \ll 1$, $\delta \ll L_0$: the final volume of the sample is almost equal to the initial volume. The concentration thus remains equal to c_0. On the opposite, for $\psi \gg 1$, $\delta \gg L_0$: the sample volume increases during the traveling time, leading to a dilution. Schematically, a dilution factor $\psi < 1$, means that the sample is not hydrodynamically diluted, while a dilution factor $\psi > 1$ means that the sample is diluted by a factor ψ. For example, for $\psi = 10$, the sample is 10 times less concentrated when it reaches the biochip surface than during its injection in the analysis system.

Equation (3) can now be amended in order to take hydrodynamic dilution into account. c_0 must be replaced by the actual concentration $c = c_0 \mathrm{erf}(1/\psi)$ when the sample reaches the

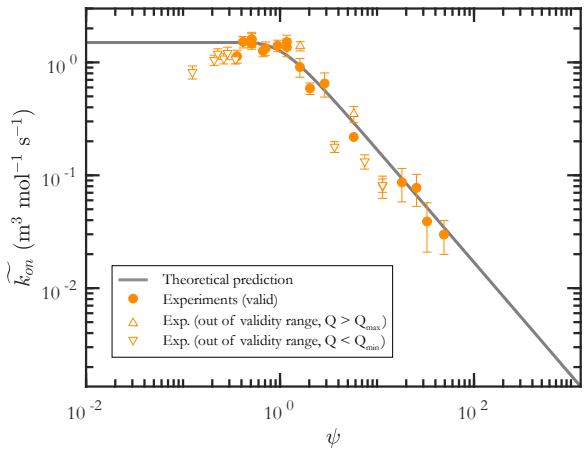

Figure 7: **Variation of the measured $\widetilde{k_{on}}$** versus the dilution factor ψ. The data points are the same as figure 3. (Solid line) Theoretical prediction $\widetilde{k_{\rm on}} = k_{\rm on}{\rm erf}(1/\psi)$. (Empty triangles) Experimental data that are out of the model validity range, either because $Q < Q_{\rm min}$ (downward pointing triangles) or $Q > Q_{\rm max}$ (upward pointing triangles) and therefore deviate from the theoretical prediction.

biochip:

$$\frac{ds}{dt} = k_{\rm on} s_m c_0 \, {\rm erf}(1/\psi) \tag{11}$$

This new equation takes into account surface complexation, as equation (3), but also the Taylor-Aris hydrodynamic dispersion, via the ψ factor we introduce (see Figure 6.b). $k_{\rm on}$ can thus be obtained by measuring the slope $\frac{ds}{dt}$ and by calculating the hydrodynamic dilution factor ψ using (9). Finally:

$$\boxed{k_{\rm on} = \frac{1}{s_m \, c_0 \, {\rm erf}(1/\psi)} \frac{ds}{dt}} \tag{12}$$

Combining equations (4) and (12) leads to

$$\widetilde{k_{\rm on}} = k_{\rm on}{\rm erf}(1/\psi) \tag{13}$$

Figure 7 shows the experimental data plotted as a function of ψ instead of Q. Remarkably, the points are very well fitted by the erf function given in equation (13), with $k_{\rm on}$ as a fitting parameter. We measure a $k_{\rm on}$ value equals 1.6 ± 0.2 mol^{-1} m^3 s^{-1}, *i.e.* with a variation

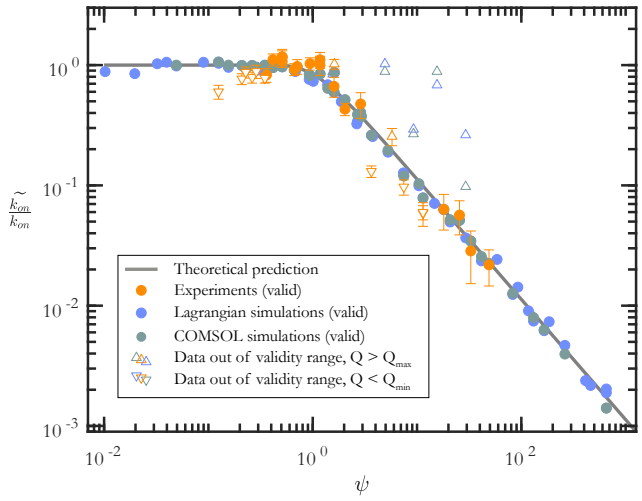

Figure 8: **Variation of the rescaled $\widetilde{k_{\mathrm{on}}}$ values versus the dilution factor ψ.** (orange points) Experimental data rescaled by the k_{on} value extracted from figure 7. (blue/grey points) Numerical data rescaled by the input k_{on} value, both from COMSOL simulations (grey) or from Lagrangian simulations (blue). (Solide line) Theoretical prediction $\frac{\widetilde{k_{\mathrm{on}}}}{k_{\mathrm{on}}} = \mathrm{erf}(1/\psi)$. (Empty triangles) Experimental or numerical data that are out of the model validity range, either because $Q < Q_{\mathrm{min}}$ (downward pointing triangles) or $Q > Q_{\mathrm{max}}$ (upward pointing triangles) and therefore deviate from the theoretical prediction.

coefficient of 12.5 %. This value is consistent with measures of other analogous biological systems obtained by several authors using the Langmuir isotherm.[2,47] This plot clearly shows that using equation (13), there is no longer variability on the k_{on} value. This work demonstrates that it is possible to take advantage of out-of-equilibrium measurements, leading to accurate results using much less sample volume than standard equilibrium measurements.

Interestingly, dividing equation (13) by k_{on} generates a universal curve, that is system independent:

$$\frac{\widetilde{k_{\mathrm{on}}}}{k_{\mathrm{on}}} = \mathrm{erf}(1/\psi) \tag{14}$$

Figure 8 displays the experimental and numerical data normalized by the k_{on} value. In order to check the universality, additional numerical results are included in this figure for Q in $[1;50,000]$ μL/min and V_0 in $[0.2;17,000]$ μL. Remarkably, most of the data collapse on a single curve, showing the universality of the approach.

Discussion on the Efficiency Enhancement

In the Langmuir isotherm method, a single measurement requires to reach equilibrium at the surface, corresponding to s_m complexes formed. The corresponding rate of complex formed is $k_{\mathrm{on}} c_0 s_m$; the time needed to reach equilibrium is thus given by $\frac{1}{k_{\mathrm{on}} c_0}$ and the required volume by $\frac{Q}{k_{\mathrm{on}} c_0}$.Using the typical values of our experiment, $k_{\mathrm{on}} = 1.6$ mol^{-1} m^3 s$^-1$, $c_0 = 50$ nm, Q = 100 μL/min, this leads to an analysis time of 3.5 h and a sample volume of 20 mL.

Using our approach, we have shown that valid measures of k_{on} could be obtained using sample volumes ranging from 2 to 500 μL and flow rates from 25 to 500 μL/min. This leads to a typical time of analysis about one minute. The gain in term of time is about 200 and in term of volume about 40 in our experimental configuration.

Discussion on Validity Range

Tube to channel geometry

Throughout the paper, we have neglected the dispersion effects in the microsystem. This assumption is valid as long as the Taylor-Aris dispersion is much larger in the capillary tubing compared to the one in the microsystem. To quantify this criterion we write the Taylor-Aris dispersion coefficient in the capillary tubing:

$$D_{TA} = \frac{Q^2}{48\pi^2 D R^2} \tag{15}$$

and in the channel with rectangular section:

$$D^*_{TA} = \frac{Q^2}{210 D W^2} \tag{16}$$

For the model to work it is therefore necessary that Taylor-Aris dispersion takes place almost only in the capillary tubing, which corresponds to:

$$\frac{D_{TA}}{D^*_{TA}} \simeq 0.44\frac{W^2}{R^2} \gg 1 \tag{17}$$

which is equivalent to work with geometrical characteristics such that $W \gg R$. In our experiments $W = 8.9$ mm and $R = 300$ μm, validating the criterion.

Flow rates

Finally, we discuss the range of validity of the method by examining the data falling outside of the model, represented by void triangles in Figures 7 and 8. Two hypothesis are important for the model to hold: 1) the plug sample diffuses following Taylor-Aris dispersion, and 2) the target complexation is not limited by the target supply to the biochip surface.

The first hypothesis requires that the target have time to diffuse along the cross-section, *i.e.* over at least a distance equal to the radius of the capillary tubing, before reaching the biochip surface.[34,35] Otherwise, the concentration profile in the capillary tubing becomes much more complex displaying a concentration profile between Figure 4.b and 4.c. This regime lies beyond the scope of the paper. The Taylor-Aris hypothesis is valid as long as the time required for the target to diffuse over a distance R is equal to, or smaller than, the time required for the sample barycenter to travel up to the biochip surface:

$$\frac{R^2}{2D} \leq \frac{(L_1 + L_0/2)\pi R^2}{Q} \tag{18}$$

This expression gives a maximum flow rate $Q_{\max}$ above which the method does not give reliable results anymore:

$$Q^{\text{theo}}_{\max} = 2\pi \left(L_1 + \frac{V_0}{2\pi R^2} \right) D$$

For flow rates above this value, the sample is expected to have no time to fully dilute via the Taylor-Aris mechanism and the measured k_{on} is found higher than expected. Experimentally, we find that the critical flow rate is about 5 times the theoretical value:

$$\boxed{Q_{\max} = 10\pi \left(L_1 + \frac{V_0}{2\pi R^2} \right) D} \tag{19}$$

Discussing the prefactor of value 5 is out of scope of the paper but previous experiments and theories highlighted enhanced diffusion due to shear[53,54] favoring such an observation. The experiments or simulations performed at flow rates above $Q_{\max}$ are depicted as empty upward pointing triangles in Figures 7 and 8. These triangles are all out of the universal curve, thus validating this criterion.

The second assumption is that the association rate constant is limited by surface complexation reaction, and not by the transport of targets up to the capture surface.

To that end, the target consumption by the biochip surface J_r must be much lower than the target flux supplying the biochip surface J_t. Extensive details are given in Squires *et al.*[55] and Amatore *et al.*[56] The authors found:

$$J_t = 1.5\, c\, W_s D \left(\frac{Q L_s^2}{D H^2 W} \right)^{1/3} \tag{20}$$

where L_s is the length of the biochip surface (along the direction of the flow), W_s its typical width, H is the microchannel height and W its width (with $W \gg H$). The reaction flux writes: $J_r = k_{\mathrm{on}} s_m c W_s L_s$. Thus, the criterion to ensure probing the association kinetics writes:

$$D_a = \frac{J_r}{J_t} = \frac{k_{\mathrm{on}} s_m\, L_s^{1/3} H^{2/3} W^{1/3}}{1.5\, D^{2/3} Q^{1/3}} \ll 1 \tag{21}$$

which is the Damköhler number. Therefore, there is a minimum flow rate below which our model no longer works:

$$\boxed{Q_{\min} = 3\,(k_{\mathrm{on}} s_m)^3\,\frac{L_s H^2 W}{D^2}} \tag{22}$$

$Q_{\min}$ was computed by taking 10 times the Q solution of the equality of (21), to ensure the validity of the inequality. For $Q < Q_{\min}$ the capture rate is limited by the target transport and not by the association, thus biasing the results. In our experimental conditions, the microfluidic system located above the biochip surface is of height $H = 1.75 \pm 0.05$ mm, width $W = 8.9 \pm 0.2$ mm, and the biochip surface length is $L_s = 1.5$ mm. Via SPRi we measure $s_m = 2.6\,10^{-7}$ mol/m^2, thus $Q_{\min} = 25\,\mu$L/min. Experimental data points that lie below this critical flow rate are represented as empty downward pointing triangles in Figures 7 and 8. They are all out of the universal curve, validating this criterion.

In conclusion, the use of the method based on equations (9) and (12) requires that the flow rate is between the values given by the equations (19) and (22).

Conclusion

This work lies in the context of the development of new out-of-equilibrium analysis techniques with a low volume of available analyte. In this article we have quantitatively demonstrated the effect of dilution of a sample by flow during its transport to the sensitive surface, both experimentally and numerically. Without a detailed analysis of these dilution effects, the classical techniques used to determine the kinetic constants give biased results. In this context we show that understanding and modelling these dilution effects allows us to work out-of-equilibrium and to determine these kinetic constants accurately. We propose a model that is easily implemented using equations (9) and (12). By using low volumes, this approach opens significant perspectives for bioanalytical applications and medical research. Indeed, many diseases, including cancer, involve slow-binding proteins, such as metalloproteins. Targeting key metalloproteins to modify their association rate is a way to slow down cancer activity.[38] Being able to measure their association kinetics and knowing the influence

of each treatment on them could lead to a great improvement in the understanding of this type of pathology, and to new treatments, more targeted, more efficient and with fewer side effects.

Conflicts of interest

There are no conflicts to declare.

Acknowledgements

This work was supported by CNRS, Université de Rennes 1, ENS de Rennes, Région Bretagne, Rennes Métropole and Agence Nationale de la Recherche (ANR) under the grant ANR-18-CE09-0029.

Supporting Information Available

Supporting information contains: 1. Targets and ligands DNA sequences, 2. Details of the numerical procedures that are used to reinforce the experimental results and the model, 3. Model used for the convection-diffusion of a sample plug.

References

(1) Dinh, T. L.; Ngan, K. C.; Shoemaker, C. B.; Walt, D. R. Using antigen-antibody binding kinetic parameters to understand single-molecule array immunoassay performance. *Anal. Chem* **2016**, *88*, 11335–11339.

(2) Kambhampati, D.; Nielsen, P. E.; Knoll, W. Investigating the kinetics of DNA-DNA and PNA-DNA interactions using surface plasmon resonance-enhanced fluorescence spectroscopy. *Biosens. Bioelectron.* **2001**, *16*, 1109–1118.

(3) Gupta, S.; Kilpatrick, P. K.; Melvin, E.; Velev, O. D. On-chip latex agglutination immunoassay readout by electrochemical impedance spectroscopy. *Lab. Chip* **2012**, *12*, 4279–4286.

(4) Tarn, M. D.; Pamme, N. *Microchip Diagnostics*; Springer, 2017; pp 69–83.

(5) Teste, B.; Malloggi, F.; Siaugue, J.-M.; Varenne, A.; Kanoufi, F.; Descroix, S. Microchip integrating magnetic nanoparticles for allergy diagnosis. *Lab. Chip* **2011**, *11*, 4207–4213.

(6) Teste, B.; Vial, J.; Descroix, S.; Georgelin, T.; Siaugue, J.-M.; Petr, J.; Varenne, A.; Hennion, M.-C. A chemometric approach for optimizing protein covalent immobilization on magnetic core–shell nanoparticles in view of an alternative immunoassay. *Talanta* **2010**, *81*, 1703–1710.

(7) Teste, B.; Kanoufi, F.; Descroix, S.; Poncet, P.; Georgelin, T.; Siaugue, J.-M.; Petr, J.; Varenne, A.; Hennion, M.-C. Kinetic analyses and performance of a colloidal magnetic nanoparticle based immunoassay dedicated to allergy diagnosis. *Anal. Bioanal. Chem.* **2011**, *400*, 3395–3407.

(8) Chandra, P.; Noh, H.-B.; Shim, Y.-B. Cancer cell detection based on the interaction between an anticancer drug and cell membrane components. *ChemComm* **2013**, *49*, 1900–1902.

(9) Tran, V.; Walkenfort, B.; König, M.; Salehi, M.; Schlücker, S. Rapid, quantitative, and ultrasensitive point-of-care testing: A portable SERS reader for lateral flow assays in clinical chemistry. *Angew. Chem. Int.* **2019**, *58*, 442–446.

(10) Zeng, X.; Andrade, C. A.; Oliveira, M. D.; Sun, X.-L. Carbohydrate–protein interactions and their biosensing applications. *Anal. Bioanal. Chem.* **2012**, *402*, 3161–3176.

(11) Song, Y.; Lin, B.; Tian, T.; Xu, X.; Wang, W.; Ruan, Q.; Guo, J.; Zhu, Z.; Yang, C. Recent progress in microfluidics-based biosensing. *Anal. Chem* **2018**, *91*, 388–404.

(12) Kim, D. C.; Kang, D. J. Molecular recognition and specific interactions for biosensing applications. *Sensors* **2008**, *8*, 6605–6641.

(13) Beavis, K. G.; Matushek, S. M.; Abeleda, A. P. F.; Bethel, C.; Hunt, C.; Gillen, S.; Moran, A.; Tesic, V. Evaluation of the EUROIMMUN Anti-SARS-CoV-2 ELISA Assay for detection of IgA and IgG antibodies. *J. Clin. Virol.* **2020**, *129*, 104468.

(14) Verma, M. S.; Tsaloglou, M.-N.; Sisley, T.; Christodouleas, D.; Chen, A.; Milette, J.; Whitesides, G. M. Sliding-strip microfluidic device enables ELISA on paper. *Biosens. Bioelectron.* **2018**, *99*, 77–84.

(15) Lee, K. H.; Zeng, H. Aptamer-based ELISA assay for highly specific and sensitive detection of Zika NS1 protein. *Anal. Chem.* **2017**, *89*, 12743–12748.

(16) Ali-Cherif, A.; Begolo, S.; Descroix, S.; Viovy, J.-L.; Malaquin, L. Programmable Magnetic Tweezers and Droplet Microfluidic Device for High-Throughput Nanoliter Multi-Step Assays. *Angew. Chem. Int. Ed.* **2012**, *124*, 10923–10927.

(17) Bobrovnik, S. Determination of antibody affinity by ELISA. Theory. *J Biochem Biophys Methods* **2003**, *57*, 213–236.

(18) MacDonald, R. A.; Hosking, C. S.; Jones, C. L. The measurement of relative antibody affinity by ELISA using thiocyanate elution. *J. Immunol. Methods* **1988**, *106*, 191–194.

(19) Stein, M.; Haselberg, R.; Mozafari-Torshizi, M.; Wätzig, H. Experimental design and measurement uncertainty in ligand binding studies by affinity capillary electrophoresis. *Electrophoresis* **2019**, *40*, 1041–1054.

(20) Voeten, R. L.; Ventouri, I. K.; Haselberg, R.; Somsen, G. W. Capillary electrophoresis: trends and recent advances. *Anal. Chem.* **2018**, *90*, 1464–1481.

(21) Krait, S.; Salgado, A.; Chankvetadze, B.; Gago, F.; Scriba, G. K. Investigation of the complexation between cyclodextrins and medetomidine enantiomers by capillary electrophoresis, NMR spectroscopy and molecular modeling. *J. Chromatogr. A* **2018**, *1567*, 198–210.

(22) Girardot, M.; Li, H.-Y.; Descroix, S.; Varenne, A. Determination of binding parameters between lysozyme and its aptamer by frontal analysis continuous microchip electrophoresis (FACMCE). *J. Chromatogr. A* **2011**, *1218*, 4052–4058.

(23) Okhonin, V.; Berezovski, M.; Krylov, S. N. Sweeping capillary electrophoresis: a non-stopped-flow method for measuring bimolecular rate constant of complex formation between protein and DNA. *J. Am. Chem. Soc.* **2004**, *126*, 7166–7167.

(24) Chu, Y.-H.; Cheng, C. Affinity capillary electrophoresis in biomolecular recognition. *Cell. Mol. Life Sci.* **1998**, *54*, 663–683.

(25) Rich, R. L.; Myszka, D. G. BIACORE J: a new platform for routine biomolecular interaction analysis. *J. Mol. Recognit.* **2001**, *14*, 223–228.

(26) Kobayashi, H.; Endo, T.; Ogawa, N.; Nagase, H.; Iwata, M.; Ueda, H. Evaluation of the interaction between β-cyclodextrin and psychotropic drugs by surface plasmon resonance assay with a Biacore® system. *J Pharm Biomed Anal* **2011**, *54*, 258–263.

(27) Leonard, P.; Hearty, S.; Ma, H.; O'Kennedy, R. *Protein Expr. Purif.*; Springer, 2017; pp 339–354.

(28) O'Shannessy, D. J.; Brigham-Burke, M.; Peck, K. Immobilization chemistries suitable for use in the BIAcore surface plasmon resonance detector. *Anal. Biochem* **1992**, *205*, 132–136.

(29) MacDonald, H.; Bonnet, H.; Van der Heyden, A.; Defrancq, E.; Spinelli, N.; Coche-Guérente, L.; Dejeu, J. Influence of aptamer surface coverage on small target recogni-

tion: A SPR and QCM-D comparative study. *J. Phys. Chem. C* **2019**, *123*, 13561–13568.

(30) Rickert, J.; Brecht, A.; Göpel, W. QCM operation in liquids: constant sensitivity during formation of extended protein multilayers by affinity. *Anal. Chem* **1997**, *69*, 1441–1448.

(31) Cheng, W.; Ding, S.; Li, Q.; Yu, T.; Yin, Y.; Ju, H.; Ren, G. A simple electrochemical aptasensor for ultrasensitive protein detection using cyclic target-induced primer extension. *Biosens. Bioelectron.* **2012**, *36*, 12–17.

(32) Gondran, C.; Dubois, M.-P.; Fort, S.; Cosnier, S.; Szunerits, S. Detection of carbohydrate-binding proteins by oligosaccharide-modified polypyrrole interfaces using electrochemical surface plasmon resonance. *Analyst* **2008**, *133*, 206–212.

(33) Hunt, H. K.; Armani, A. M. Label-free biological and chemical sensors. *Nanoscale* **2010**, *2*, 1544–1559.

(34) Taylor, G. I. Dispersion of soluble matter in solvent flowing slowly through a tube. *Proc. R. Soc. A* **1953**, *219*, 186–203.

(35) Aris, R. On the dispersion of a solute in a fluid flowing through a tube. *Proc. R. Soc. A* **1956**, *235*, 67–77.

(36) Abrantes, M.; Magone, M. T.; Boyd, L. F.; Schuck, P. Adaptation of a surface plasmon resonance biosensor with microfluidics for use with small sample volumes and long contact times. *Anal. Chem* **2001**, *73*, 2828–2835.

(37) Guo, F.; Fu, Q.; Zhou, K.; Jin, C.; Wu, W.; Ji, X.; Yan, Q.; Yang, Q.; Wu, D.; Li, A., et al. Matrix metalloprotein-triggered, cell penetrating peptide-modified star-shaped nanoparticles for tumor targeting and cancer therapy. *J. Nanobiotechnology* **2020**, *18*, 1–16.

(38) Lee, C.-Y.; Yang, S.-F.; Wang, P.-H.; Su, C.-W.; Hsu, H.-F.; Tsai, H.-T.; Hsiao, Y.-H. Antimetastatic effects of Terminalia catappa leaf extracts on cervical cancer through the inhibition of matrix metalloprotein-9 and MAPK pathway. *Environ* **2019**, *34*, 60–66.

(39) Liu, Y.; Wang, C. Predicting cracks in metalloproteins. *Nat. Mach. Intell.* **2019**, *1*, 553–554.

(40) Yang, Y.; Hu, X.-Q.; Li, Q.-S.; Zhang, X.-X.; Ruan, B.-F.; Xu, J.; Liao, C. Metalloprotein inhibitors for the treatment of human diseases. *Curr. Top. Med. Chem.* **2016**, *16*, 384–396.

(41) Oh, S.; Kang, D.; Ahn, S.-M.; Simpson, R. J.; Lee, B.-H.; Moon, M. H. Miniaturized asymmetrical flow field-flow fractionation: Application to biological vesicles. *J. Sep. Sci.* **2007**, *30*, 1082–1087.

(42) Rouffet, M.; Cohen, S. M. Emerging trends in metalloprotein inhibition. *Dalton Trans.* **2011**, *40*, 3445–3454.

(43) Jonsson, U.; Fagerstam, L.; Ivarsson, B.; Johnsson, B.; Karlsson, R.; Lundh, K.; Lofas, S.; Persson, B.; Roos, H.; Ronnberg, I., et al. Real-time biospecific interaction analysis using surface plasmon resonance and a sensor chip technology. *Biotechniques* **1991**, *11*, 620–627.

(44) Karlsson, R.; Michaelsson, A.; Mattsson, L. Kinetic analysis of monoclonal antibody-antigen interactions with a new biosensor based analytical system. *J. Immunol. Methods* **1991**, *145*, 229–240.

(45) Maillart, E. Imagerie par résonance des plasmons de surface pour l'analyse simultanée de multiples intéractions biomoléculaires en temps réel. Ph.D. thesis, 2004.

(46) Yuan, B.-f.; Zhuang, X.-y.; Hao, Y.-h.; Tan, Z. Kinetics of base stacking-aided DNA hybridization. *ChemComm* **2008**, 6600–6602.

(47) Liebermann, T.; Knoll, W.; Sluka, P.; Herrmann, R. Complement hybridization from solution to surface-attached probe-oligonucleotides observed by surface-plasmon-field-enhanced fluorescence spectroscopy. *Colloids Surf, A Physicochem Eng Asp* **2000**, *169*, 337–350.

(48) Gotoh, M.; Hasegawa, Y.; Shinohara, Y.; Shimizu, M.; Tosu, M. A new approach to determine the effect of mismatches on kinetic parameters in DNA hybridization using an optical biosensor. *DNA Res.* **1995**, *2*, 285–293.

(49) Kuzmichev, A.; Skolnik, J.; Zybin, A.; Hergenröder, R. Absolute analysis of nanoparticle suspension with surface plasmon microscopy. *Anal. Chem* **2018**, *90*, 10732–10737.

(50) Peh, W. Y.; Reimhult, E.; Teh, H. F.; Thomsen, J. S.; Su, X. Understanding ligand binding effects on the conformation of estrogen receptor α-DNA complexes: A combinational quartz crystal microbalance with dissipation and surface plasmon resonance study. *Biophys. J.* **2007**, *92*, 4415–4423.

(51) Young, M.; Carroad, P.; Bell, R. Estimation of diffusion coefficients of proteins. *Biotechnol. Bioeng.* **1980**, *22*, 947–955.

(52) Smith, M. H. *Molecular weights of proteins and some other materials including sedimentation, diffusion, and frictional coefficients and partial specific volumes*; CRC Press, 2018; p 74.

(53) Mary, P.; Studer, V.; Tabeling, P. Microfluidic droplet-based liquid- liquid extraction. *Anal. Chem* **2008**, *80*, 2680–2687.

(54) Salmon, J.-B.; Ajdari, A. Transverse transport of solutes between co-flowing pressure-driven streams for microfluidic studies of diffusion/reaction processes. *EJ-Physics* **2007**, *101*, 074902.

(55) Squires, T. M.; Messinger, R. J.; Manalis, S. R. Making it stick: convection, reaction and diffusion in surface-based biosensors. *Nat. Biotechnol* **2008**, *26*, 417.

(56) Amatore, C.; Da Mota, N.; Sella, C.; Thouin, L. Theory and experiments of transport at channel microband electrodes under laminar flows. 1. Steady-state regimes at a single electrode. *Anal. Chem* **2007**, *79*, 8502–8510.

For Table of Contents Only

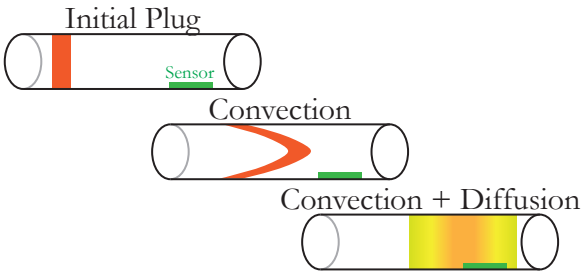

How to extract k_{on} from the sensorgram?